mater.scichina.com link.springer.com

Published online 30 May 2022 | https://doi.org/10.1007/s40843-022-2053-5
Sci China Mater 2022, 65(10): 2704–2710

Ultrasmall Ag nanoclusters anchored on NiCo-layered double hydroxide nanoarray for efficient electrooxidation of 5-hydroxymethylfurfural

Jing Jin, Yingyan Fang, Tianyu Zhang, Aijuan Han, Bingqing Wang* and Junfeng Liu*

ABSTRACT **Electrochemical oxidation of 5-hydroxymethylfurfural (HMF) has shown promising prospects in producing highly valuable chemicals. Herein, we report the synthesis of ultrasmall Ag nanoclusters anchored on NiCo-layered double hydroxide (NiCo-LDH) nanosheet arrays (Ag_n@NiCo-LDH) *via* a facile electrodeposition strategy. The prepared Ag_n@NiCo-LDH nanosheet arrays exhibit excellent electrocatalytic HMF oxidation performance with a current density of 10 mA cm^{-2} at 1.29 V_{RHE} and the Faraday efficiency of nearly 100% for 2,5-furandicarboxylic acid production. This study offers an effective approach to rationally design nanoclusters to achieve high catalytic activity for sustainable energy conversion and production.**

Keywords: ultrasmall Ag nanoclusters, layered double hydroxides, nanosheet array, electrodeposition, 5-hydroxymethylfurfural electrooxidation

INTRODUCTION

Biomass conversion into value-added chemicals is an important and desirable way to reduce the depletion of fossil fuels and improve energy utilization efficiency [1–4]. 5-Hydroxymethylfurfural (HMF) is one of the most extensively studied biomass-derived platform molecules, serving as a promising candidate for driving numerous high-value chemicals by oxidizing its furan ring, aldehyde, and alcohol groups [5–7]. Of particular importance is the oxidation product 2,5-furandicarboxylic acid (FDCA) [8], acting as a precursor for the production of bio-polymer polyethylene furanoate (PEF) [9] and a large-scale monomer of commercial polyethylene terephthalate [10]. Given the broad demand for FDCA in industry, immense efforts have been made to study the catalytic synthesis of FDCA from HMF [11]. Traditionally, the conversion of HMF to FDCA depends on thermocatalytic processes that require harsh reaction conditions (high temperature and pressure) and expensive catalysts [12,13]. In contrast, the electrochemical synthesis is a thriving alternative method in which the oxidation is driven by the applied potential under mild conditions [14]. However, the electrooxidation of HMF in alkaline media always competes with the oxygen evolution reaction (OER) ($4OH^- \rightarrow O_2 + 2H_2O + 4e^-$) [15–18], resulting in a low Faraday efficiency (FE) for HMF oxidation [19]. Hence, it is crucial to rationally design electrocatalysts to increase the FE and reduce the driven potential, as well as achieve the high yield of FDCA for HMF oxidation.

Currently, most studies on HMF electro-oxidation are focused on heterogeneous electrocatalysts [13,20]. Noble metal-based catalysts, including Pt [21], Pd [22], Au [23], Ru [24], and Ag-based [25] catalysts, have been widely studied for HMF electro-oxidation because of their unique electron and orbital properties [26]. Considering the metal particle size as a key factor in performance evaluation, downsizing the metal particle is of great importance in introducing more uncoordinated atoms and enhancing the metal-support interaction [27,28]. Once the metal is downsized to nano or sub-nano scale, its catalytic behavior could change dramatically [29]. Particularly, ultrasmall metal nanoclusters with low-nuclearity metal atoms can considerably expose the active centers while retaining the metallic properties [30–32]. As the intermediate states between single-atom catalysts and nanoparticles, supported nanoclusters can provide enough sites for the adsorption and activation of multiple substrates with a relatively high atom utilization efficiency, thus reducing the reaction barrier and increasing the catalytic activity [33–36]. For instance, highly dispersed Pt clusters supported on a metal-organic framework (MOF) displayed high catalytic activity for photocatalytic H_2 production [37]. Gold nanocluster catalyst promoted the electrochemical production of ammonia derived from the electronic interaction between Au nanoclusters and supports [38]. Therefore, such metal nanoclusters could exhibit great potential to improve the HMF electro-oxidation performance. Specifically, Ag has the lowest price among the above mentioned noble-metal catalysts [39]; however, few studies have been done on HMF electro-oxidation by using Ag nanoclusters as the electrocatalyst to date, and the synthesis of Ag nanoclusters also remains a challenge because of the high surface energy of ultrasmall metal nanoclusters.

Herein, we report the rational design and synthesis of Ag nanoclusters anchored on NiCo-layered double hydroxide (LDH) (Ag_n@NiCo-LDH) nanosheet arrays for highly efficient HMF oxidation. LDHs were chosen as the support due to their adjustable components and flexible structures, thus benefiting the performance optimization [40,41]. Particularly, the Ni- and Co-containing LDHs possess variable valence states of metal ions, further enhancing the metal-support interaction [42–44]. The Ag_n@NiCo-LDH nanosheet arrays were prepared *via* a facile electrochemical deposition strategy, which showed great potential in managing the particle size [45]. The obtained Ag_n@NiCo-LDH catalyst exhibited excellent catalytic performance in HMF electro-oxidation reaction, achieving a nearly 100% yield (>98%) and FE (>97%) for FDCA production at the applied potential of 1.39 V *vs.* reversible hydrogen electrode

State Key Laboratory of Chemical Resource Engineering, Beijing University of Chemical Technology, Beijing 100029, China
* Corresponding authors (emails: ljf@mail.buct.edu.cn (Liu J); wangbq0698@163.com (Wang B))

(RHE) without any sacrificial agents. Moreover, the Ag_n@NiCo-LDH catalyst also showed considerable durability and stability, thus demonstrating its potential as a biotransformation catalyst. This work offers an effective approach to rationally design nanoclusters to achieve high catalytic activity for sustainable energy conversion and production.

EXPERIMENTAL SECTION

Synthesis of NiCo-LDH nanosheet array

The NiCo-LDH nanosheet nanoarray was prepared by a facile electrodeposition method. In a typical procedure, a piece of nickel foam (NF, 2 cm × 2 cm) was cleaned with HCl solution (6 mol L^{-1}) by ultrasonication for 5 min to remove the surface NiO layer and subsequently sonicated in deionized (DI) water and absolute ethanol for 3 min, respectively. Later, the clean NF was used as the working electrode, and the Ag/AgCl electrode and Pt plate were used as the reference and counter electrodes, respectively, for the electrochemical deposition. An aqueous solution containing $Ni(NO_3)_2{\cdot}6H_2O$ (0.1 mol L^{-1}) and $Co(NO_3)_2{\cdot}6H_2O$ (0.1 mol L^{-1}) was used as the deposition electrolyte. The NiCo-LDH nanosheet array was obtained on the working electrode under a constant deposition potential of −1.0 V *vs*. Ag/AgCl electrode for 10 min, and finally rinsed with DI water and ethanol thrice.

Synthesis of Ag_n@NiCo-LDH nanosheet array

The Ag_n@NiCo-LDH nanosheet array was prepared through an electrochemical deposition process in a standard three-electrode system. Typically, the as-prepared NiCo-LDH nanosheet array was used as the working electrode, and the Ag/AgCl electrode and Pt plate were used as the reference and counter electrodes, respectively. A solution containing 100 μmol L^{-1} $AgNO_3$ and 1 mol L^{-1} KOH was used as the electrolyte. The electrochemical deposition was performed *via* cyclic voltammetry (CV) from 0.1 to 0.8 V *vs*. Ag/AgCl electrode with a sweeping rate of 5 mV s^{-1} for two cycles. After the deposition, the electrode was washed with DI water thrice.

Material characterization

Sample morphology was characterized *via* field-emission scanning electron microscopy (Zeiss SUPRA 55) and transmission electron microscopy (TEM, Hitachi HT7700). The high-resolution TEM (HRTEM) and energy-dispersive X-ray spectroscopy (EDX) were performed on a JEOL JEM-2100F. Aberration-corrected high-angle annular dark-field scanning TEM (AC-HAADF-STEM) images were obtained using a JEOL JEM-ARM200F TEM/STEM with a spherical aberration corrector working at 300 kV. X-ray diffraction (XRD) was performed on an RIGAKU XRD-6000A diffractometer at 40 kV and 100 mA with copper-filtered Kα radiation (λ = 1.5406 Å). X-ray photoelectron spectroscopy (XPS) was performed on a model of ESCALAB 250. The binding energies were calibrated by referring C 1s peak to 284.8 eV. X-ray absorption fine structure (XAFS) measurements were performed at the BL14W1 beamline, Shanghai Synchrotron Radiation Facility (SSRF, energy 3.5 GeV, current 250 mA maximum, Si (311) double crystals as double-crystal monochromator covering the photon energy range of 8.5–50 keV). The loading amount of Ag on the 1 cm × 1 cm electrode was determined by an inductively coupled plasma atomic emission spectrometer (ICP-AES). The catalytic products were analyzed *via* high-performance liquid chromatography (HPLC, Shimadzu Prominence LC-2030C system) equipped with an ultraviolet (UV)-visible detector.

Electrochemical measurements

All electrochemical measurements were conducted on a CHI 660E electrochemical station (Shanghai Chenhua, China) with a conventional three-electrode configuration at ambient temperature. Saturated Ag/AgCl and platinum plate electrodes served as the reference and counter electrodes, respectively. The Ag_n@NiCo-LDH nanosheet arrays were directly used as the working electrode. The potentials were referenced to the RHE (E_{RHE} = $E_{Ag/AgCl}$ + 0.2412 + 0.0591pH). Linear sweep voltammetry (LSV) was measured at a scan rate of 5 mV s^{-1} with 85% *iR* compensation. Electrochemical impedance spectroscopy (EIS) tests were measured over a frequency range of 10^5 to 10^{-2} Hz with the alternating current (AC) amplitude of 10 mV. A constant potential electrolysis test was conducted in a divided cell separated by the Nafion 117 membrane. The HMF oxidation products were analyzed *via* HPLC with a UV-visible detector. The UV detector wavelength was set to 265 nm. The mobile phase A of HPLC was methanol, and phase B was 5 mmol L^{-1} ammonium formate aqueous solution. The ratio of A:B was 3:7, and the flow rate was 0.6 mL min^{-1}. In each measurement, a 20-μL sample was drawn from the electrolyte during the potentiostatic electrolysis and diluted to 1 mL with ultrapure water and analyzed *via* HPLC. The conversion of HMF, FDCA yield, and FE were calculated according to Equations (1–3), respectively.

$$\text{HMF conversion (\%)} = \frac{n(\text{HMF consumed})}{n(\text{HMF initial})} \times 100, \quad (1)$$

$$\text{FDCA yield (\%)} = \frac{n(\text{FDCA})}{n(\text{HMF initial})} \times 100, \quad (2)$$

$$\text{FE (\%)} = \frac{n(\text{FDCA})}{\text{Charge}/(6\times F)} \times 100, \quad (3)$$

where F is the Faraday constant (96,485 C mol^{-1}), and n is the mole amount of the reactant calculated from the HPLC concentration analysis.

RESULTS AND DISCUSSION

The fabrication strategy of the Ag_n@NiCo-LDH nanosheet arrays was schematically shown in Scheme 1. The vertically aligned NiCo-LDH nanosheets on NF were first prepared as the support *via* a facile electrosynthesis method (Fig. S1). Then, Ag species were deposited on the NiCo-LDH nanosheet arrays during the CV cycling process in the electrolyte containing $AgNO_3$. As shown in Fig. 1a, the obtained Ag_n@NiCo-LDH nanosheets were uniformly distributed on the NF without any morphology change in NiCo-LDH after the loading of Ag species. The TEM image in Fig. 1b confirms the nanosheet characteristic of Ag_n@NiCo-LDH, without an obvious aggregation of silver. The Ag species in Ag_n@NiCo-LDH were further investigated *via* AC-HAADF-STEM. As shown in Fig. 1c and Fig. S2, after two cycles of CV electrochemical deposition, a significant number of clusters (marked by red circles) were observed, indicating the dispersion of Ag species on NiCo-LDH as about 1.5 nm-sized ultrasmall nanoclusters. However, increasing the CV electrochemical deposition to four or ten cycles, Ag nanoclusters continually grew into larger nanoparticles with a

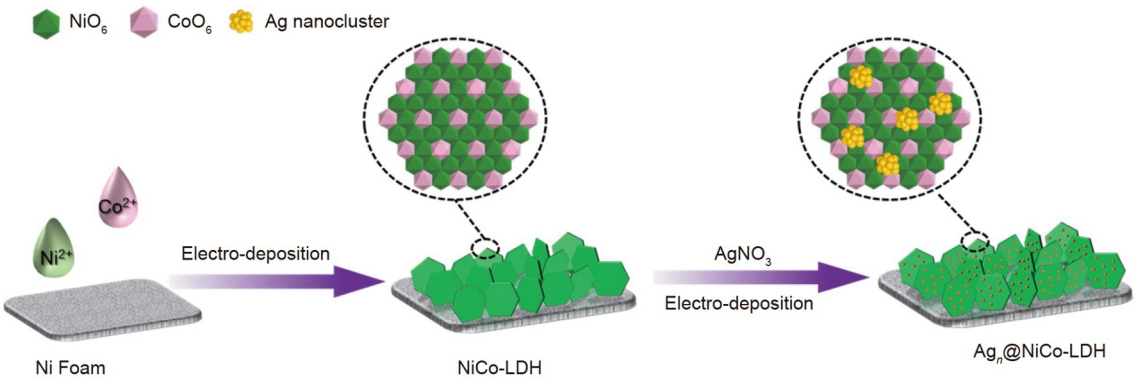

Scheme 1 Schematic illustration of the fabrication process of Ag_n@NiCo-LDH nanosheet arrays.

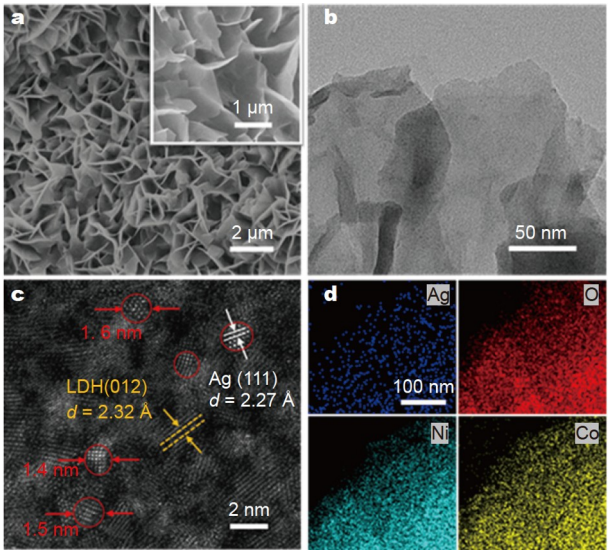

Figure 1 Morphology characterizations of the Ag_n@NiCo-LDH nanosheet arrays. (a) Low- and high-magnification (inset) SEM images; (b) TEM; (c) AC-HAADF-STEM, and (d) EDX mapping images of Ag_n@NiCo-LDH nanosheets.

size range of about 4 to 10 nm (Fig. S3). Besides, the lattice plane distances of 2.27 and 2.32 Å were attributed to the (111) crystal plane of Ag and the (012) plane of the LDH phase, respectively. EDX mapping showed that the Ag, O, Ni, and Co elements were homogeneously dispersed over the entire architecture (Fig. 1d).

ICP-AES analysis revealed that the silver content in Ag_n@NiCo-LDH was ~0.3 wt%, consistent with the EDX result (Fig. S4). XRD patterns of Ag_n@NiCo-LDH and NiCo-LDH exhibited a series of (00*l*) peaks which matched well with those of NiCo-LDH (JPCDS No. 33-0429) without any impurity peaks (Fig. 2a). No peaks of Ag bulk (JPCDS No. 304-0783) were observed in the patterns of Ag_n@NiCo-LDH, indicating the well-dispersed Ag on NiCo-LDH and small-sized Ag nanoclusters. XAFS measurement was further employed to accurately acquire the local structure and coordination environment of Ag species. As shown in the Ag K-edge X-ray absorption near-edge structure (XANES) spectra in Fig. 2b, the Ag absorption edge of Ag_n@NiCo-LDH was located between the Ag foil and Ag_2O, suggesting that the oxidation state of Ag nanoclusters in Ag_n@NiCo-LDH was between 0 and +1. Meanwhile, Fourier transforms of k^2-weighted extended XAFS (EXAFS) spectra for Ag_n@NiCo-LDH in R space exhibited the main peak at 2.71 Å, corresponding to the Ag–Ag interaction, indicating the predominant metallic Ag feature in Ag_n@NiCo-LDH (Fig. 2c). In addition, a weak peak at 1.67 Å could be assigned to the Ag–O coordination, indicating that the Ag nanoclusters were coordinated with O atoms on NiCo-LDH with partial Ag atoms in a valence state of +1, consistent with the Ag K edge XANES spectrum. To determine the precise atomic structure and explore the interaction between the Ag nanoclusters and NiCo-LDH support, the EXAFS curve fitting of Ag_n@NiCo-LDH was performed (Fig. S5 and Table S1). According to the fitting results, the first coordination shell of Ag–Ag was observed at 2.71 Å with a coordination number of 6, suggesting the formation of Ag clusters. Besides, the Ag–O bond at 1.67 Å with a coordination number of 4 suggested that the Ag nanoclusters were stabilized by the bridging O atoms of NiCo-LDH. XPS was further employed to characterize the chemical composition and electronic properties of Ag_n@NiCo-LDH. The full XPS spectra of NiCo-LDH revealed signals of Ni, Co, O, and C elements. After the Ag electrodeposition, the signal of the Ag element was observed in the full XPS spectra of Ag_n@NiCo-LDH (Fig. S6). The high-resolution XPS spectra of Ag 3d of Ag_n@NiCo-LDH showed four main peaks (Fig. 2d), where the peaks at 373.3 and 367.3 eV could be assigned to Ag^+, and those at 374.8 and 368.8 eV indicated the presence of metallic silver [46–48]. The oxidation state of Ag in Ag_n@NiCO-LDH was higher than zero, which was consistent with the XAFS results [49]. The valence states of Co and Ni in Ag_n@NiCo-LDH and NiCo-LDH were further analyzed to explore the potential interaction between the Ag nanoclusters and support. As shown in Fig. 2e, compared with the prinstine NiCo-LDH, the binding energy of Co $2p_{2/3}$ in Ag_n@NiCo-LDH exhibited a positive shift from 780.5 to 780.9 eV, and the atomic ratio of Co^{3+}/Co^{2+} decreased from 1.37 to 1.02 compared with that of pristine NiCo-LDH. Meanwhile, the binding energy of Ni 2p of Ag_n@NiCo-LDH barely changed compared with that of the pristine NiCo-LDH (Fig. 2f). These results suggest an electron transfer from Ag nanoclusters to Co atoms in Ag_n@NiCo-LDH.

The electrocatalytic HMF oxidation performance of the as-prepared Ag_n@NiCo-LDH was evaluated in an H-type (proton exchange membrane) electrochemical cell using 1 mol L^{-1} KOH as the electrolyte at ambient temperature. The electrochemical measurement was performed in a standard three-electrode configuration using a commercial Pt plate and Ag/AgCl as the counter and reference electrodes, respectively (Fig. 3a). A con-

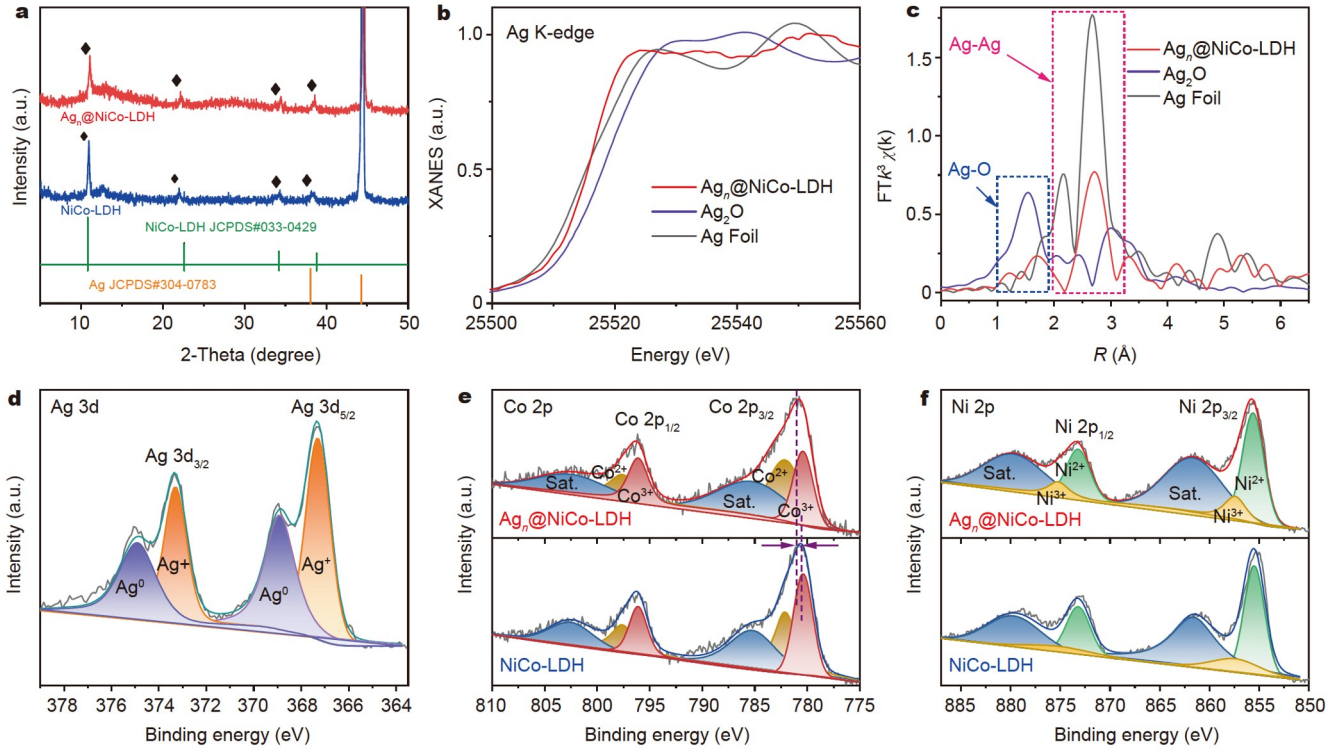

Figure 2 (a) XRD patterns of Ag$_n$@NiCo-LDH and NiCo-LDH (the sharp diffraction peak at 44.5° belonged to the Ni foam substrate). Ag K-edge (b) XANES profiles and (c) EXAFS spectra in R space for Ag$_n$@NiCo-LDH, Ag$_2$O, and Ag foil. HR-XPS spectra of (d) Ag 3d, (e) Co 2p, and (f) Ni 2p of Ag$_n$@NiCo-LDH and NiCo-LDH.

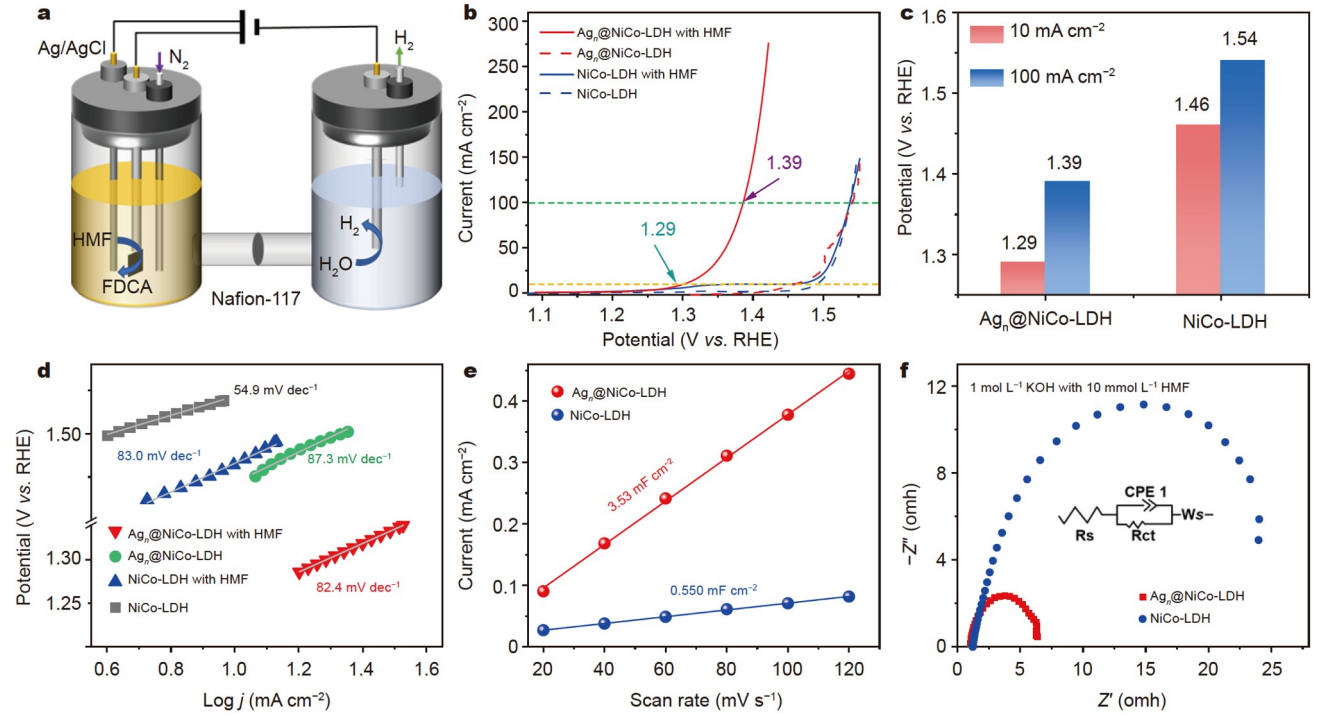

Figure 3 (a) Schematic diagram of the electrochemical system used for HMF oxidation with cathode and anode. (b) LSV curves of electrocatalysts at a scan rate of 5 mV s^{-1} in 1 mol L^{-1} KOH with or without adding 10 mmol L^{-1} HMF. (c) HMF oxidation potentials at current densities of 10 and 100 mA cm^{-2} for Ag$_n$@NiCo-LDH and NiCo-LDH and (d) the corresponding Tafel plots. (e) Capacitive currents at –0.20 V *vs.* Ag/AgCl electrode as a function of the scan rate for Ag$_n$@NiCo-LDH and NiCo-LDH. (f) The Nyquist plots of Ag$_n$@NiCo-LDH and NiCo-LDH in 1 mol L^{-1} KOH with 10 mmol L^{-1} HMF.

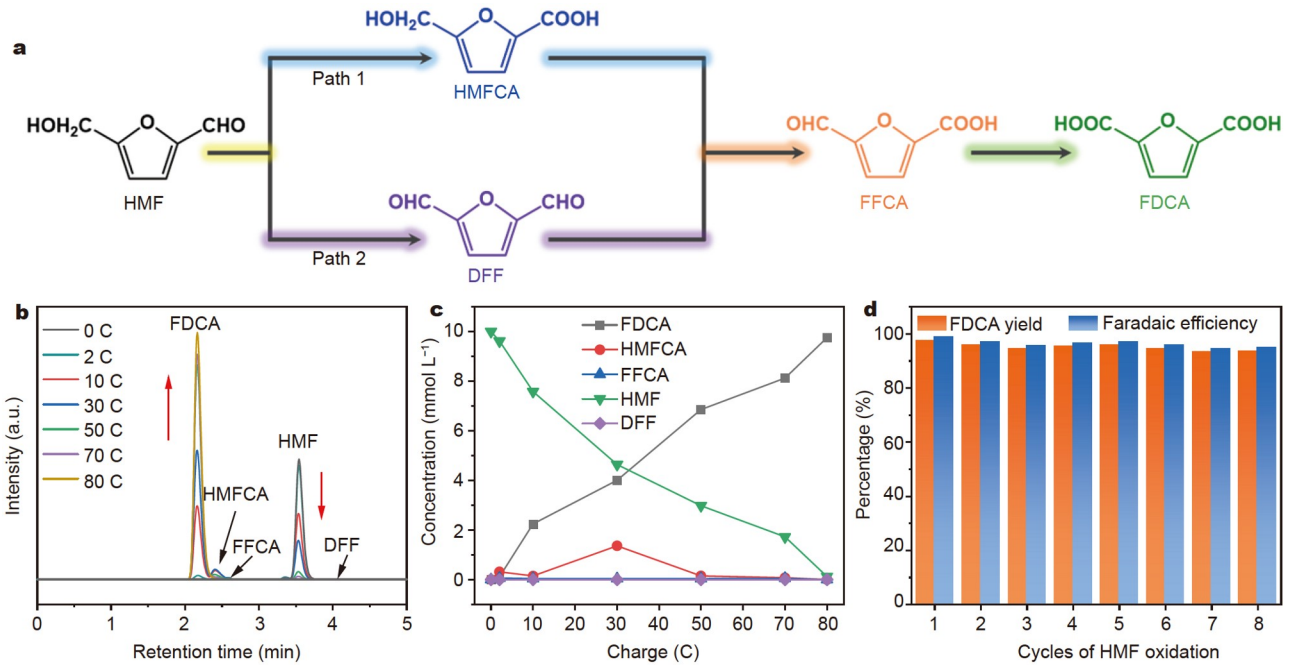

Figure 4 (a) Schematic illustration of the two possible HMF oxidation pathways to FDCA. (b) HPLC chromatograms at various passed charge states during electrolysis. (c) Plots of concentration *versus* passed charge of HMF, FDCA, and the intermediates during the electrochemical oxidation of HMF over Ag_n@NiCo-LDH. (d) Yield and FE (%) of FDCA obtained by Ag_n@NiCo-LDH for eight consecutive cycles in HMF oxidation.

stant potential electrolysis test was conducted in a divided cell separated by the Nafion 117 membrane. Fig. 3b depicts the LSV curves of Ag_n@NiCo-LDH and NiCo-LDH with or without HMF (10 mmol L^{-1}) in the electrolyte. Notably, OER is the main competing reaction during the HMF oxidation. Without HMF in the electrolyte, the Ag_n@NiCo-LDH showed an onset potential (at 5 mA cm^{-2}) of 1.43 V *vs.* RHE for OER in 1 mol L^{-1} KOH, slightly lower than that of NiCo-LDH (1.47 V *vs.* RHE). After adding 10 mmol L^{-1} HMF into the electrolyte, the onset potential (at 5 mA cm^{-2}) of Ag_n@NiCo-LDH reduced to 1.28 V *vs.* RHE, indicating that the oxidation of HMF on Ag_n@NiCo-LDH was much easier than OER. However, the onset potential of NiCo-LDH showed negligible change on HMF addition, suggesting that the ultrasmall Ag nanoclusters promoted the HMF electro-oxidation process. Moreover, the applied potentials at 10 and 100 mA cm^{-2} were tested as important evaluation parameters for this reaction. As shown in Fig. 3c, the Ag_n@NiCo-LDH only needed 1.29 and 1.39 V (*vs.* RHE) to reach the current densities of 10 and 100 mA cm^{-2}, respectively, much lower than those of NiCo-LDH (1.46 and 1.54 V *vs.* RHE) and most developed electrodes (Table S2). The relatively low driving potential at high current density indicates that it is promising for practical applications. In addition, Tafel slope kinetics for OER and HMF oxidation over Ag_n@NiCo-LDH and NiCo-LDH were calculated by the linear fitting of polarization curves. As shown in Fig. 3d, the Tafel slope for HMF oxidation over Ag_n@NiCo-LDH was lower than that for OER (82.4 *vs.* 87.3 mV dec^{-1}), demonstrating better kinetics of HMF oxidation on Ag_n@NiCo-LDH. In contrast, the Tafel slope for OER was 54.9 mV dec^{-1} and increased to 83.0 mV dec^{-1} in the presence of HMF over NiCo-LDH, suggesting the inactive nature of NiCo-LDH for HMF oxidation. To investigate the origin of the superior HMF oxidation performance of Ag_n@NiCo-LDH, we further measured the electrochemically active surface area during HMF oxidation, which was linearly proportional to the double-layer capacitance (C_{dl}). Using the CV method at the non-Faradaic region of −0.22 to −0.18 V *vs.* Ag/AgCl electrode, the electrochemically active surface area could be calculated from the linear relationship between the current densities at −0.20 *vs.* Ag/AgCl electrode and scan rates (Fig. S7). Based on these curves, the C_{dl} value of Ag_n@NiCo-LDH was 3.53 mF cm^{-2}, seven times higher than that of NiCo-LDH (0.55 mF cm^{-2}), indicating that Ag_n@NiCo-LDH provided more electrocatalytically active sites for HMF oxidation (Fig. 3e). Moreover, the EIS was also measured. Ag_n@NiCo-LDH showed a smaller charge transfer resistance than NiCo-LDH catalysts, further demonstrating its much higher catalytic activity (Fig. 3f). In addition, the Ag loading on NiCo-LDH was optimized. As shown in Fig. S8, Ag_n@NiCo-LDH with the Ag loading of 0.3 wt% exhibited the highest catalytic activity among other electrocatalysts (Ag_n@NiCo-LDH-1, Ag_n@NiCo-LDH-4 and Ag_n@NiCo-LDH-10).

Generally, there are two possible pathways of HMF oxidation to FDCA owing to the presence of aldehyde and hydroxyl groups in HMF (Fig. 4a). The first step of HMF oxidation is the conversion of HMF to 5-hydroxymethyl-2-furancarboxylic acid (HMFCA, Path 1) or 2,5-diformylfuran (DFF, Path 2). Then, the generated HMFCA and DFF are oxidized to 5-formyl-2-furancarboxylic acid (FFCA) and finally, FDCA. To better understand the kinetics of the catalytic HMF oxidation over Ag_n@NiCo-LDH, constant potential oxidation of HMF to FDCA was performed. The oxidation products (HMFCA, DFF, FFCA, and FDCA) in the electrolyte were determined *via* HPLC. The calibration curves were obtained by plotting the peak areas of standard substances with five different concentrations (Fig. S9). Fig. 4b shows the chromatograms of the reactant and product at different charges. The peak attributed to HMF at the retention

time of 3.54 min continuously decreased in intensity, while the signal of FDCA at the retention time of 2.16 min gradually increased as the reaction progressed. Moreover, the intermediate product DFF (4.10 min) was not detected, and the concentration of HMFCA increased gradually. The above results implied that the main path of HMF oxidation over Ag_n@NiCo-LDH was Path 1, wherein HMF was preferentially oxidized at the aldehyde groups. Fig. 4c shows the conversion and concentration changes of HMF over different charges. When the passing charge reached 80 C, the peak belonging to HMF in the HPLC spectrum almost disappeared, while that belonging to FDCA increased to the maximum. The corresponding FDCA yield and FE were obtained at 97.5% and 98.8% at this number of electron consumption (80 C), respectively, indicating the high activity and selectivity of Ag_n@NiCo-LDH toward electrocatalytic HMF oxidation. In addition, the Ag_n@NiCo-LDH electrode also showed considerable durability for HMF oxidation. The yield and FE toward FDCA demonstrated no obvious change after eight cycle reactions (Fig. 4d).

CONCLUSIONS

In summary, ultrasmall Ag nanoclusters anchored on NiCo-LDH (Ag_n@NiCo-LDH) nanosheet arrays were successfully prepared *via* the electrodeposition method, exhibiting excellent catalytic performance in the electrooxidation of HMF into FDCA, surpassing most developed catalysts. This study demonstrates a promising approach for biomass conversion into high value-added chemicals by using LDH-supported nanoclusters as catalysts, which provides a new platform for the exploration of biotransformation catalysts.

Received 13 February 2022; accepted 23 March 2022; published online 30 May 2022

1 Sudarsanam P, Zhong R, Van den Bosch S, *et al.* Functionalised heterogeneous catalysts for sustainable biomass valorisation. Chem Soc Rev, 2018, 47: 8349–8402
2 Isikgor FH, Becer CR. Lignocellulosic biomass: A sustainable platform for the production of bio-based chemicals and polymers. Polym Chem, 2015, 6: 4497–4559
3 Xu X, Guo T, Xia J, *et al.* Modulation of the crystalline/amorphous interface engineering on Ni-P-O-based catalysts for boosting urea electrolysis at large current densities. Chem Eng J, 2021, 425: 130514
4 Guo T, Xu XJ, Wang X, *et al.* Enabling the full exposure of Fe_2P@Ni_xP heterostructures in tree-branch-like nanoarrays for promoted urea electrolysis at high current densities. Chem Eng J, 2021, 417: 128067
5 Huang X, Song J, Hua M, *et al.* Enhancing the electrocatalytic activity of CoO for the oxidation of 5-hydroxymethylfurfural by introducing oxygen vacancies. Green Chem, 2020, 22: 843–849
6 Zhu W, Meng Y, Yang C, *et al.* Effect of coordination environment surrounding a single Pt site on the liquid-phase aerobic oxidation of 5-hydroxymethylfurfural. ACS Appl Mater Interfaces, 2021, 13: 48582–48594
7 Xiang K, Wu D, Deng X, *et al.* Boosting H_2 generation coupled with selective oxidation of methanol into value-added chemical over cobalt hydroxide@hydroxysulfide nanosheets electrocatalysts. Adv Funct Mater, 2020, 30: 1909610
8 Hayashi E, Yamaguchi Y, Kamata K, *et al.* Effect of MnO_2 crystal structure on aerobic oxidation of 5-hydroxymethylfurfural to 2,5-furandicarboxylic acid. J Am Chem Soc, 2019, 141: 890–900
9 Motagamwala AH, Won W, Sener C, *et al.* Toward biomass-derived renewable plastics: Production of 2,5-furandicarboxylic acid from fructose. Sci Adv, 2018, 4: eaap9722
10 Chen C, Wang L, Zhu B, *et al.* 2,5-Furandicarboxylic acid production *via* catalytic oxidation of 5-hydroxymethylfurfural: Catalysts, processes and reaction mechanism. J Energy Chem, 2021, 54: 528–554
11 Chen L, Shi J. Co-electrolysis toward value-added chemicals. Sci China Mater, 2022, 65: 1–9
12 Chimentão RJ, Oliva H, Belmar J, *et al.* Selective hydrodeoxygenation of biomass derived 5-hydroxymethylfurfural over silica supported iridium catalysts. Appl Catal B-Environ, 2019, 241: 270–283
13 Zhao Y, Cai M, Xian J, *et al.* Recent advances in the electrocatalytic synthesis of 2,5-furandicarboxylic acid from 5-(hydroxymethyl)furfural. J Mater Chem A, 2021, 9: 20164–20183
14 Prabhu P, Wan Y, Lee JM. Electrochemical conversion of biomass derived products into high-value chemicals. Matter, 2020, 3: 1162–1177
15 Wang B, Han X, Guo C, *et al.* Structure inheritance strategy from MOF to edge-enriched NiFe-LDH array for enhanced oxygen evolution reaction. Appl Catal B-Environ, 2021, 298: 120580
16 Zhang J, Liu C, Zhang B. Insights into single-atom metal-support interactions in electrocatalytic water splitting. Small Methods, 2019, 3: 1800481
17 Song C, Liu Y, Wang Y, *et al.* Highly efficient oxygen evolution and stable water splitting by coupling NiFe LDH with metal phosphides. Sci China Mater, 2021, 64: 1662–1670
18 Wang D, Chang YX, Li YR, *et al.* Well-dispersed $NiCoS_2$ nanoparticles/rGO composite with a large specific surface area as an oxygen evolution reaction electrocatalyst. Rare Met, 2021, 40: 3156–3165
19 Bai XJ, He WX, Lu XY, *et al.* Electrochemical oxidation of 5-hydroxymethylfurfural on ternary metal-organic framework nanoarrays: Enhancement from electronic structure modulation. J Mater Chem A, 2021, 9: 14270–14275
20 Gu K, Wang D, Xie C, *et al.* Defect-rich high-entropy oxide nanosheets for efficient 5-hydroxymethylfurfural electrooxidation. Angew Chem, 2021, 133: 20415–20420
21 Vuyyuru KR, Strasser P. Oxidation of biomass derived 5-hydroxymethylfurfural using heterogeneous and electrochemical catalysis. Catal Today, 2012, 195: 144–154
22 Chadderdon DJ, Xin L, Qi J, *et al.* Electrocatalytic oxidation of 5-hydroxymethylfurfural to 2,5-furandicarboxylic acid on supported Au and Pd bimetallic nanoparticles. Green Chem, 2014, 16: 3778–3786
23 Cha HG, Choi KS. Combined biomass valorization and hydrogen production in a photoelectrochemical cell. Nat Chem, 2015, 7: 328–333
24 Zheng L, Zhao J, Du Z, *et al.* Efficient aerobic oxidation of 5-hydroxymethylfurfural to 2,5-furandicarboxylic acid on Ru/C catalysts. Sci China Chem, 2017, 60: 950–957
25 German D, Pakrieva E, Kolobova E, *et al.* Oxidation of 5-hydroxymethylfurfural on supported Ag, Au, Pd and bimetallic Pd-Au catalysts: Effect of the support. Catalysts, 2021, 11: 115
26 Du Y, Sheng H, Astruc D, *et al.* Atomically precise noble metal nanoclusters as efficient catalysts: A bridge between structure and properties. Chem Rev, 2020, 120: 526–622
27 Li Z, Wu R, Zhao L, *et al.* Metal-support interactions in designing noble metal-based catalysts for electrochemical CO_2 reduction: Recent advances and future perspectives. Nano Res, 2021, 14: 3795–3809
28 Ma Z, Tian H, Meng G, *et al.* Size effects of platinum particles@CNT on HER and ORR performance. Sci China Mater, 2020, 63: 2517–2529
29 Zhu Y, Zhao W, Zhang J, *et al.* Selective activation of C–OH, C–O–C, or C=C in furfuryl alcohol by engineered Pt sites supported on layered double oxides. ACS Catal, 2020, 10: 8032–8041
30 Peng M, Dong C, Gao R, *et al.* Fully exposed cluster catalyst (FECC): Toward rich surface sites and full atom utilization efficiency. ACS Cent Sci, 2021, 7: 262–273
31 Dong C, Li Y, Cheng D, *et al.* Supported metal clusters: Fabrication and application in heterogeneous catalysis. ACS Catal, 2020, 10: 11011–11045
32 Ji S, Chen Y, Zhao S, *et al.* Atomically dispersed ruthenium species inside metal-organic frameworks: Combining the high activity of atomic sites and the molecular sieving effect of MOFs. Angew Chem, 2019, 131: 4315–4319
33 Rong H, Ji S, Zhang J, *et al.* Synthetic strategies of supported atomic clusters for heterogeneous catalysis. Nat Commun, 2020, 11: 5884
34 Han X, Zhang T, Chen W, *et al.* Mn-N_4 oxygen reduction electrocatalyst: *Operando* investigation of active sites and high performance in

zinc-air battery. Adv Energy Mater, 2021, 11: 2002753
35 Wang H, Liu JX, Allard LF, *et al.* Surpassing the single-atom catalytic activity limit through paired Pt-O-Pt ensemble built from isolated Pt_1 atoms. Nat Commun, 2019, 10: 3808
36 Han A, Wang B, Kumar A, *et al.* Recent advances for MOF-derived carbon-supported single-atom catalysts. Small Methods, 2019, 3: 1800471
37 Huang X, Li X, Luan Q, *et al.* Highly dispersed Pt clusters encapsulated in MIL-125-NH_2 *via in situ* auto-reduction method for photocatalytic H_2 production under visible light. Nano Res, 2021, 14: 4250–4257
38 Tan Y, Yan L, Huang C, *et al.* Fabrication of an Au_{25}-cys-Mo electrocatalyst for efficient nitrogen reduction to ammonia under ambient conditions. Small, 2021, 17: 2100372
39 Zhang N, Zhang X, Tao L, *et al.* Silver single-atom catalyst for efficient electrochemical CO_2 reduction synthesized from thermal transformation and surface reconstruction. Angew Chem Int Ed, 2021, 60: 6170–6176
40 Dong L, Chang GR, Feng Y, *et al.* Regulating Ni site in NiV LDH for efficient electrocatalytic production of formate and hydrogen by glycerol electrolysis. Rare Met, 2022, 41: 1583–1594
41 Chu B, Ma Q, Li Z, *et al.* Design and preparation of three-dimensional hetero-electrocatalysts of NiCo-layered double hydroxide nanosheets incorporated with silver nanoclusters for enhanced oxygen evolution reactions. Nanoscale, 2021, 13: 11150–11160
42 Gao R, Yan D. Fast formation of single-unit-cell-thick and defect-rich layered double hydroxide nanosheets with highly enhanced oxygen evolution reaction for water splitting. Nano Res, 2018, 11: 1883–1894
43 Gao R, Zhu J, Yan D. Transition metal-based layered double hydroxides for photo(electro)chemical water splitting: A mini review. Nanoscale, 2021, 13: 13593–13603
44 Gao R, Yan D. Recent development of Ni/Fe-based micro/nanostructures toward photo/electrochemical water oxidation. Adv Energy Mater, 2020, 10: 1900954
45 Zhang Z, Feng C, Liu C, *et al.* Electrochemical deposition as a universal route for fabricating single-atom catalysts. Nat Commun, 2020, 11: 1215
46 Kim SH, Choi WI, Kim KH, *et al.* Nanoscale chemical and electrical stabilities of graphene-covered silver nanowire networks for transparent conducting electrodes. Sci Rep, 2016, 6: 33074
47 Ye L, Liu J, Gong C, *et al.* Two different roles of metallic Ag on Ag/AgX/BiOX (X = Cl, Br) visible light photocatalysts: Surface plasmon resonance and *Z*-scheme bridge. ACS Catal, 2012, 2: 1677–1683
48 Yang H, Zhang X, Yu Y, *et al.* Manganese vacancy-confined single-atom Ag in cryptomelane nanorods for efficient wacker oxidation of styrene derivatives. Chem Sci, 2021, 12: 6099–6106
49 Li R, Xu X, Zhu B, *et al. In situ* identification of the metallic state of Ag nanoclusters in oxidative dispersion. Nat Commun, 2021, 12: 1406

Acknowledgements This work was financially supported by the National Natural Science Foundation of China (21975013) and the Fundamental Research Funds for the Central Universities. The authors thank the BL14W1 station at Shanghai Synchrotron Radiation Facility (SSRF).

Author contributions Jin J performed the experiments, collected and analyzed the data, and wrote the paper. Zhang T and Han A discussed the results. Fang Y assisted with the electrochemical tests. Liu J and Wang B conceived the experiments, analyzed results, and wrote the paper. All authors discussed the results and commented on the manuscript.

Conflict of interest The authors declare that they have no conflict of interest.

Supplementary information Experimental details and supporting data are available in the online version of the paper.

Jing Jin is a PhD candidate at the School of Chemistry, Beijing University of Chemical Technology, under the supervision of Prof. Junfeng Liu. Her research focuses on the design and synthesis of nanocatalysts for organic electrocatalysis.

Bingqing Wang is a postdoctor at the Department of Chemistry, Tsinghua University. He received his PhD degree from the School of Chemistry, Beijing University of Chemical Technology in 2019. He is interested in the synthesis of MOFs, nanoclusters, and single-atom catalysts, as well as their electrochemical and organic catalytic applications.

Junfeng Liu received her BSc degree and PhD degree in chemistry from Tsinghua University in 2002 and 2007, respectively. She joined the State Key Laboratory of Chemical Resource Engineering, Beijing University of Chemical Technology, in 2008. Her main research interests focus on functional inorganic materials and their applications in catalysis and energy field.

NiCo水滑石阵列负载的Ag团簇用于高效电催化氧化5-羟甲基糠醛

金晶, 方莺燕, 张天宇, 韩爱娟, 王兵庆*, 刘军枫*

摘要 将生物质转化为燃料和高附加值化学品具有重要意义. 电催化氧化5-羟甲基糠醛是将生物质转化为燃料和高附加值化学品的一条重要途径. 本文通过简便的电沉积方法制备了一种NiCo水滑石纳米阵列负载的Ag纳米团簇(Ag_n@NiCo-LDH)自支撑电极材料. 在碱性介质中, 所制备的Ag_n@NiCo-LDH自支撑电极表现出了优异的电催化氧化5-羟甲基糠醛的活性和循环稳定性. 在电压为1.29 V条件下, 电流密度可达10 mA cm^{-2}, 2,5-呋喃二甲酸(FDCA)产率高达97.5%, 法拉第效率为98.8%. 本工作为高效能源转化催化剂的设计提供了新思路。

